Journal of Oil Palm Research Vol. 36 (4) December 2024 p. 687-707
DOI: https://doi.org/10.21894/jopr.2024.0004

COMPOSITE OF ZnO/SBE AS CATALYST MATERIALS FOR PHOTODEGRADATION OF RHODAMINE-B

DIAH SUSANTI[1]*; SHAFIRA MARELLIA[1]; AZZAH DYAH PRAMATA[1]; I D A A WARMADEWANTHI[2]; ERVIN NURHAYATI[2]; HANIFFUDIN NURDIANSAH[1] and JHY-CHERN LIU[3]

ABSTRACT

Spent Bleaching Earth (SBE) is a solid waste material from the palm oil refining process, and its abundance poses environmental challenges. Meanwhile, Rhodamine B (RhB) is a liquid pollutant produced by the textile industry. SBE could potentially be a viable solution for RhB treatment, as it can adsorb on its surface. However, SBE lacks the ability to chemically degrade the RhB pollutant. Therefore, in this study, SBE was combined with zinc oxide (ZnO), a highly effective photocatalyst semiconductor, to create a composite material for the photodegradation of RhB. This experiment aimed to investigate the effect of SBE pyrolysis temperature on the morphology and structure of the ZnO/SBE composite, as well as its capability to degrade RhB. The pyrolysis temperatures chosen for variation were 450°C, 500°C, and 550°C. The experiments have shown that SBE activated at 500°C exhibited the highest surface area, measuring 106.851 m^2 g^{-1}. Consequently, the corresponding composite ZnO/SBE photocatalyst activated at 500°C demonstrated the most efficient performance in RhB degradation, achieving a rate of 67.8%. The ability of ZnO/SBE to photodegrade RhB was confirmed by the GC-MS results, which demonstrated the degradation of RhB into various other chemicals.

Keywords: photodegradation, pyrolysis, Rhodamine-B, SBE, ZnO.

Received: 8 May 2023**; Accepted:** 23 October 2023**; Published online:** 9 January 2024.

INTRODUCTION

The textile industry is a significant contributor to pollutant production, with 8000 kg of cloth produced globally in 2019 (Pinto *et al.*, 2019). One of the main sources of textile pollutants is textile colouring agents, which contain organic compounds that are not easily degraded in nature (Dianggoni *et al.*, 2017). Rhodamine B (RhB) is a commonly used synthetic dye in the textile industry due to its affordability, accessibility, and vibrant red colour (Aristanti *et al.*, 2019). However, RhB is known to be harmful to both human health and the environment, necessitating appropriate pollutant treatment methods to prevent pollution. One environmentally friendly method is adsorption (Bahram *et al.*, 2014), which involves binding molecules in fluids to solid surfaces (Yustinah *et al.*, 2019). However, adsorption alone does not degrade the dyes and requires an additional process, such as photodegradation, to achieve complete degradation (Trivana *et al.*, 2015).

Photodegradation is a process in which molecules are degraded through the absorption of photons from light (photo) (Yousif and Haddad, 2013). Zinc oxide (ZnO), a semiconductor material, is a potential photocatalyst that can be used to facilitate the photodegradation process (Khan *et al.*, 2022). ZnO offers several advantages, including low production costs, non-toxicity, and widespread availability (Cambrussi *et al.*, 2019). However, ZnO

---

[1] Materials and Metallurgical Engineering Department,
Institut Teknologi Sepuluh Nopember (ITS),
Kampus ITS, Keputih, Sukolilo, Surabaya, 60111 Indonesia.

[2] Environmental Engineering Department,
Institut Teknologi Sepuluh Nopember (ITS),
Kampus ITS, Keputih, Sukolilo, Surabaya, 60111 Indonesia.

[3] Chemical Engineering Department,
National Taiwan University of Science and Technology (NTUST),
Sec. 4 No. 43, Keelung Road, Taipei, 106335 Taiwan-ROC.

* *Corresponding author e-mail: santiche@mat-eng.its.ac.id*

has a limitation in terms of its low adsorption capacity (Saraswati *et al*., 2015).

Spent Bleaching Earth (SBE), a waste product from the crude palm oil (CPO) bleaching process, can be utilised for adsorption due to its porous characteristics. However, activation is required to enhance its adsorption capacity, typically achieved by using mineral acids such as hydrochloric acid (HCl), sulphuric acid (H_2SO_4), or nitric acid (HNO_3) (Lesaoana *et al*., 2019). Liu *et al.* (2021) conducted research on the synergistic carbonisation of residual oil in SBE and the activation process of SBE using KOH, resulting in the creation of a novel clay (SBE)/carbon composite. This composite was then employed as an effective adsorbent for the removal of Pb^{2+} (Liu *et al*., 2021). The carbon produced through the carbonisation process is commonly referred to as 'biochar' (Foong *et al*., 2022).

The amount of solid SBE waste from palm oil production is increasing significantly every year. According to the Ministry of Environment and Forestry in the Republic of Indonesia, for every 600 million tonnes of palm oil produced, there is an estimated 600 000 t of solid SBE waste generated (Kementerian Lingkungan Hidup dan Kehutanan Republik Indonesia, 2020). It is worth noting that SBE still contains a significant amount of valuable palm oil, ranging from 25% to 40%. As a result, it is highly flammable and poses a risk of causing fires (Lee *et al*., 2000). Therefore, it is essential to handle the disposal of SBE with utmost care to prevent any adverse impact on the environment.

SBE is a group of montmorillonite clay, in which montmorillonite is a typical of aluminosilicate of 2:1 layered structure. The structure theoretically composed of two silicon tetra oxide (SiO_4) tetrahedral layers sandwiched with one aluminum dioxide tetra hydroxide [$AlO_2(OH)_4$] octahedral layer making it a member of phyllosilicates family. Montmorillonite is known for its exceptional adsorption properties, high active surface area, and ability to exchange ions or molecules. The ions or molecules exchange capabilities were influenced by isomorphous substitutions of lower-valent metal cations, such as Al^{3+} to substitute Si^{4+} in the tetrahedral layer and Mg^{2+} to substitute Al^{3+} in octahedral layer. Hence the surface structure of montmorillonite is negatively charged and can attract positively charged cations, such as Fe^{2+}, Ca^{2+}, Mg^{2+}, and Na^{2+}, to balance the surface charge (Chen *et al*., 2022a; Ferreira *et al*., 2019; Sani *et al*., 2017).

Montmorillonite has great capacity to accommodate new species and assist in the formation of product through chemical reactions. Due to its unique properties, montmorillonite has various applications. Besides being used as a chemical reaction catalyst, it serves as an excellent adsorbent for diverse purposes, including waste water treatment, pollutant removal, oil bleaching processes, and radioactive waste management. Moreover, montmorillonite can act as a support material for other substances, such as ZnO and g-C_3N_4, to enhance the material functionality, such as for photocatalyst (Chen *et al*, 2022a; Sani *et al*, 2017).

Pyrolysis is a thermochemical technique employed to decompose lignocellulosic materials or biomass, primarily for the purpose of activation. This process transpires in an environment devoid of oxygen or with controlled oxygen concentrations, resulting in the creation of a substance referred to as biochar. Biochar is a solid product distinguished by its elevated carbon content (Faramarzi *et al*., 2015; Foong *et al*, 2022; Sukiran *et al*., 2018). During pyrolysis, volatile matter from the biomass evaporates, leading to increased porosity and active surface area of the material (Fu *et al*., 2020). The temperature during pyrolysis is critical as it determines the pyrolysis rate and the amount of lost volatile matter (Hu and Gholizadeh, 2019).

Pyrolysis can be categorised into two main types: Slow pyrolysis and fast pyrolysis. Slow pyrolysis is characterised by a gradual heating rate, typically ranging from 0.02 to 1.00°C s^{-1}, and an extended residence period spanning from several hours to days occurring within 300°C-700°C. In contrast, fast pyrolysis involves a rapid heating rate exceeding 2.00°C s^{-1} and a much shorter residence time of less than 10 s occurring within 300°C-1000°C (Foong *et al*., 2021).

Previous studies by the authors' research group have shown that SBE activated through pyrolysis at 500°C resulted in a surface area of 158.7 $m^2\ g^{-1}$ (Rizqiyah, *et al*., 2022). Other research reported that SBE when further activated with KOH, exhibited an adsorption rate of 206.65 mg g^{-1} for Pb^{2+} (Liu *et al*., 2021). Similarly, Chen *et al*. (2022b) activated iron-based SBE at 700°C, resulting in a surface area of 90.98 $m^2\ g^{-1}$ and a degradation efficiency of 91.0% for tetracycline hydrochloride. Therefore, pyrolysis proves to be effective in activating SBE by opening the pores and removing impurities.

ZnO/SBE composites offer several advantages as photocatalyst materials for dye degradation, such as enhanced photocatalytic activity, improved adsorption capacity, cost-effectiveness, and environmental friendliness. However, they also have some limitations, including limited visible-light absorption, photocorrosion and stability issues, recyclability challenges, and potential substrate compatibility concerns.

Numerous studies have been conducted on the photocatalytic degradation and removal of colorant/dye wastes, leading to significant achievements. For instance, Hindryawati *et al*. (2020) investigated the photocatalytic degradation of methylene blue (MB) using SBE impregnated with WO_3, while Saputra *et al*. (2020) studied the photocatalytic degradation of MB with $CeFeO_3$/calcinated SBE. In another investigation, Slamet *et al*. (2021) explored the application of SBE/ZnO composite for the removal of RhB, comparing its adsorption ability in both dark and ambient light conditions. Furthermore, Rahayu and Nurhayati (2023) compared the adsorption capacities of SBE and activated SBE for RhB dye. Additionally, Yulikasari, *et al.* (2023) employed SBE/ZnO in a catalytic ozonation process to remove RhB. However, it is essential to note that the methods used in the reported studies differ from those in this research.

Another avenue of research involves the application of semiconductor and montmorillonite composite materials for photodegrading RhB. Haounati *et al*. (2023) demonstrated the use of ZnO/montmorillonite photocatalyst in RhB degradation under UV light irradiation and the presence of scavenger agents. Similarly, Djellabi *et al*. (2014) employed a TiO_2/montmorillonite composite for RhB photodegradation under UV-A irradiation. Notably, the reported studies utilised fresh montmorillonite, whereas this research focuses on spent montmorillonite (SBE).

Despite extensive efforts to find studies employing the same materials, pollutant, and methodology, there was a lack of research on the photocatalytic degradation of RhB using ZnO/SBE. Consequently, this study remains relatively rare and presents ample opportunities for further development and exploration.

Furthermore, the papers reported by other groups seldom mention the examination of the photodegradation products. According to the mass conservation law, mass cannot be created nor destroyed; it simply transfers from one substance to another. As a result, it is crucial to conduct meticulous observations to identify the products formed after the photocatalytic process. This study has taken the initiative to identify these products using gas chromatography-mass spectrometry (GC-MS).

By focusing on the identification of the photodegradation products, this work aims to shed light on the complete mechanism of the photocatalytic process and provide valuable insights into the fate of the reactants and the formation of new substances. This comprehensive understanding is essential in assessing the efficiency and environmental impact of photocatalytic applications. Hence, this research not only explores the photodegradation process but also demonstrates a novel approach to examining the photodegradation products using GC-MS, offering valuable contributions to the field, and laying the foundation for further exploration in this area.

In this research, a composite material consisting of SBE and ZnO was synthesised for use as a photocatalyst in the photodegradation process of RhB. The variable studied was the pyrolysis temperature, which was set at 450°C, 500°C, and 550°C for activating SBE. The structure, morphology, active surface area, and chemical composition of SBE, ZnO, and ZnO/SBE composites were characterised using various material characterisation techniques. The photocatalytic performance of the synthesised materials was evaluated through photocatalytic tests. The correlations between pyrolysis temperatures and the chemical and physical properties of the materials were investigated, as well as their effects on the photocatalytic performance. At the end of the research, an investigation of the photodegradation products was conducted using GC-MS instrumentation. This analytical technique was utilised to identify the substances produced during the photocatalytic process.

MATERIALS AND METHODS

Prior to the activation process, as received or pure SBE was characterised using Scanning Electron Microscope (SEM), X-Ray Diffractometer (XRD), Fourier-Transformed Infra-Red (FTIR), and Brunauer-Emmet-Teller (BET) instruments. To start the activation process of SBE, a total of 1000 g of pure SBE was dried at 200°C for 10 hr in a muffle furnace, followed by soaking in 0.1 M KOH for 24 hr to decompose organic impurities such as the remaining CPO in SBE. The SBE was then dried in a vacuum oven at room temperature for 12 hr. The dried SBE was subjected to pyrolysis under a nitrogen flow in a horizontal vacuum furnace at temperatures of 450°C, 500°C and 550°C for 2 hr. The resulting pyrolysed SBE samples were washed with 2 M HCl and distilled water until neutral (pH = 7), dried at 200°C for 10 hr in a muffle furnace, and then filtered using 100 mesh filter paper. At the end of these processes the activated SBE was produced. The volatile matter compositions of the pyrolysed samples were examined following the American Society for Testing Materials (ASTM) D-3174 procedure (Isnugroho *et al*., 2016). The SBE samples activated at 450°C, 500°C and 550°C were denoted as ASBE1, ASBE2 and ASBE3, respectively.

The synthesis of the ZnO/SBE composite involved dissolving 78.7 g of zinc acetate dihydrate ($Zn(CH_3CO_2)_2{\cdot}2H_2O$) in 337.5 mL of distilled water and then mixing it with 120 mL of ethanol. The complete formation of ZnO can be described by the following reaction in Equation (1) (Ha *et al*., 2013).

$$Zn(CH_3COOH)_2.2H_2O_{(s)} + 2NaOH_{(aq)} \longrightarrow ZnO_{(s)} + 2NaCH_3COO_{(aq)} + H_2O_{(l)} \quad (1)$$

Subsequently, 12.5 g of activated SBE was added to the solution. The mixture was refluxed at 80°C for 2 hr and then transferred to a 1000 mL glass beaker, where 225 mL of 2 M NaOH was added while stirring with a magnetic stirrer for 1 hr to form a gel composed of wet precipitate. The precipitate was filtered using 100 mesh filter paper, and the resulting ZnO/SBE composite precipitate was dried in a vacuum oven at 60°C for 12 hr. The composite material formed by combining activated SBE (ASBE) with ZnO was designated as KSBE. Specifically, KSBE1, KSBE2 and KSBE3 were used to represent the composites of ASBE1, ASBE2 and ASBE3 with ZnO, respectively.

The structure, morphology, and composition of the materials were characterised using X-ray diffractometer (XRD Panalytical X'pert Cu Ka = 1.5406 Å), Scanning Electron Microscope equipped with Energy Dispersive X-Ray Spectrometer (SEM/EDX, FEI Tecnai S50) and Fourier Transformed Infra-Red (FTIR Shimadzu) instrument, respectively. The active surface area was measured using a Brunauer-Emmet-Teller (BET Quantachrome Nova 4200e) instrument and the photocatalytic test results were measured using a UV-Vis spectrophotometer (Thermo Fischer Scientific Genesys) and GC-MS (Perkin Elmer) instrument.

Photocatalytic testing was performed to analyse the effect of SBE activation temperature on the performance of ZnO/SBE composite (KSBE) in degrading RhB. Standard RhB solutions with concentrations of 2, 4, 6, 8, 10, and 12 ppm were prepared to build a linear curve showing the correlation between absorbance and concentration values. A 12 ppm RhB solution was then mixed with 0.5 g of SBE in a 50 mL beaker glass, which was tightly covered and irradiated using a 20 W TL blue light source (Philips TL blue light 20 W/52 l = 400 - 500 nm, peak l = 450 nm) for varying durations of 0, 2, 4, 6, 8, and 10 hr. This process was repeated for the photocatalyst materials, including ZnO, KSBE1 (450°C), KSBE2 (500°C), and KSBE3 (550°C). Each sample was measured using a UV-Vis instrument every 2 hr, and the absorbance data were converted into concentration in ppm.

Before conducting the photocatalytic measurements on each material, the RhB solution was pre-conditioned in the dark with the photocatalyst materials, namely SBE, ZnO, KSBE1, KSBE2 or KSBE3. This pre-conditioning step aimed to ensure that the adsorption of RhB reached equilibrium prior to exposing it to UV irradiation. By doing so, it could be confirmed that any reduction in RhB absorption observed was solely attributed to photodegradation rather than the adsorption of RhB in the ZnO/SBE composite.

RESULTS AND DISCUSSION

Figure 1a shows the X-ray diffraction peaks of the samples SBE, ASBE1, ABSE2 and ASBE3, which consist of quartz and montmorillonite (Al_2O_3, SiO_2, CaO, and Fe_2O_3) phases (Yulikasari *et al*., 2022). The findings were in line with the characteristics of SBE which is classified as a group of montmorillonite clay (Sabour and Shahi, 2018). The SiO_2 diffraction peaks are observed at 2θ = 20.7°, 21.5°, 26.5°, 27.3°, 39.3°, 59.7° and 68°, corresponding to (110), (002), (022), (141), (321), and (262) planes, respectively, as per JCPDS 46-1045 (Amritphale *et al*., 2016). The diffraction peaks of Al_2O_3 are observed at 2θ = 35.4°, 42.2°, 43.1° and 47.3°, corresponding to (200), (202), (024) and (213) planes, respectively, as per JCPDS 12-0219 (Yulikasari *et al*., 2022). Fe_2O_3 peaks are observed at 2θ = 27.6°, 29.1° and 45.7°, corresponding to (121), (112), and (231) planes, respectively, according to International Crystallographic Diffraction Data (ICDD) No. 01-089-0597 (Ilmi *et al*., 2021). The diffraction peak of CaO is observed at 49.9° for the (143) plane, as per JCPDS No. 82-1691 (Singh *et al*., 2018).

Figure 1b shows the diffraction patterns of ZnO and activated ZnO/SBE composites. In addition to the diffraction patterns shown in *Figure 1a* there are diffraction peaks of ZnO observed at 2θ = 30.90°, 31.71°, 34.30°, 36.14°, 47.34°, 56.51° and 62.67° which correspond to (100), (002), (101), (102), (110), (103), (112) and (201) planes, respectively, according to JCPDS card 36-1451 (Nurbayasari and Saridewi, 2017). Based on the XRD diffraction peaks, the crystallite size of the materials was calculated using the Scherrer formula, and the results were summarised in *Table 1*.

The Scherrer formula for calculating crystallite size is given by (Cullity and Stock, 2014):

$$d = \frac{K\lambda}{B \cos \theta} \qquad (2)$$

where, d is the crystallite size (nm), K is the constant (taken as 0.9), λ is the X-ray wavelength Cu K-α source = 0.15406 nm, B is the breadth or full width at half maximum (radian) and θ is the diffraction angle (radian).

The crystallite sizes of SBE, ASBE1, ASBE2 and ASBE3 materials were calculated to be 127.5, 72.8, 56.6 and 102.0 nm, respectively. Similarly, the crystallite sizes of ZnO, KSBE1, KSBE2 and KSBE3 were found to be 61.2, 65.2, 57.9 and 57.9 nm, respectively. Interestingly, the crystallite sizes of ZnO decreased upon composite formation with ASBE, possibly due to reduced inter-atomic collisions caused by the presence of ASBE, as suggested by previous studies (Septiani *et al*., 2014). Notably, there were significant changes in the crystallite sizes of SBE before and after the activation process, indicating a structural transformation. In general, the SBE pyrolysed at 500°C exhibited the smallest crystallite size.

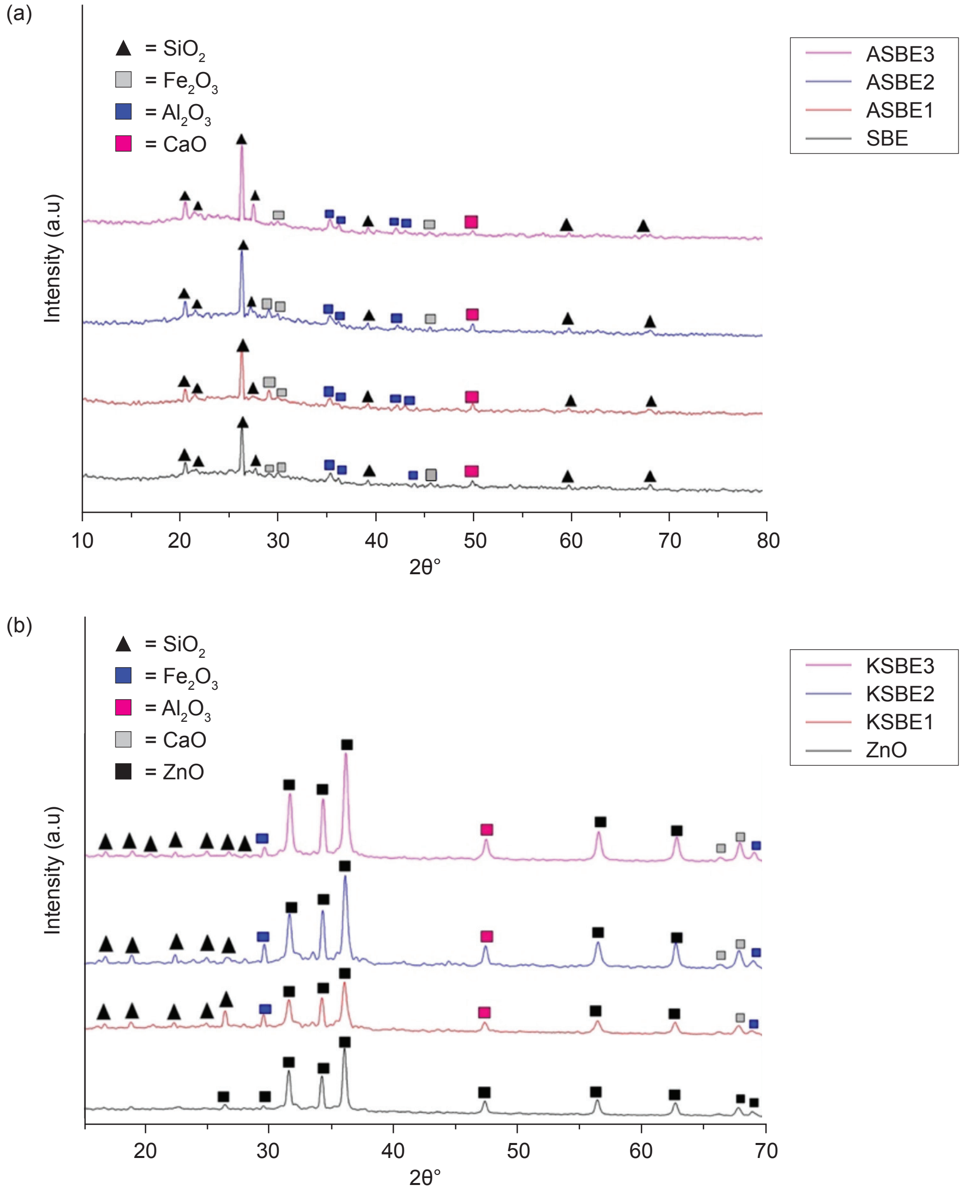

Figure 1. XRD results of (a) SBE, ASBE1, ASBE2 and ASBE3, (b) ZnO, KSBE1, KSBE2 and KSBE3.

TABLE 1. THE CRYSTALLITE SIZE OF THE SAMPLES WAS CALCULATED USING DEBBYE-SCHERRER FORMULA

No.	Sample	2θ°	FWHM (rad)	Crystallite size (nm)	$d_{spacing}$ (Å) SBE	$d_{spacing}$ (Å) ZnO
1	SBE	26.6214	0.0669	127.5	3.344	-
2	ASBE1	26.4618	0.1171	72.8	3.370	-
3	ASBE2	26.4396	0.1506	56.6	3.368	-
4	ASBE3	26.4480	0.0836	102.0	3.371	-
5	ZnO	36.2141	0.1428	61.2	-	2.478
6	KSBE1	36.0449	0.1338	65.2	3.368	2.62
7	KSBE2	36.0696	0.1506	57.9	3.37	2.49
8	KSBE3	36.1714	0.1506	57.9	3.36	2.48

As reported by Mana *et al.* (2011) on the TGA/DSC of SBE, there was a sharp TG decreasing curve corresponding to ~ 42% mass loss from room temperature to 500°C which was attributed to the evaporation of water content (represented by an exothermic peak at 278°C), the release of volatile products or remaining oil, and the decomposition as well as the burning of organic matters (represented by two exothermic peaks at 341°C and 400°C). After 500°C to 800°C, the TG curve sloped and the mass loss was only ~2%. The DSC curve also showed an endothermic peak at 500°C which was attributed to the breakage of the hydroxyl group. Hence, the crystallite size of SBE pyrolysed at 500°C was the smallest due to the greatest mass loss of impurities from room temperature to 500°C. The loss of impurities caused the SBE to restructure the atomic arrangement nearly to the structure of pure BE. The energy given in the form of high pyrolysis temperature was used to erase the impurities. However, when the temperature increased to more than 500°C, the remaining energy was used to decompose further the material and enlarge the crystallite size as well.

The lattice spacing ($d_{spacing}$) of material can be calculated using Bragg's law [Equation (3)] which is expressed as follows (Cullity and Stock, 2014):

$$d_{spacing} = \frac{n\lambda}{2 \sin \theta} \tag{3}$$

In which, $d_{spacing}$ is the lattice spacing (Å), λ is the X-ray wavelength Cu K-a source = 0.15406 nm, θ is the diffraction angle (°), n is the integer number (1, 2, 3, *etc.*).

The lattice spacings of the materials are presented in *Table 1*. For SBE, the lattice spacing was calculated from the SiO_2 peak at 2θ = 26.6214°, resulting in a value of 3.344 Å. This value closely matched the SiO_2 lattice spacing of SiO_2 (quartz) with a trigonal crystal structure, which is 3.34347 Å (Heriyanti *et al*., 2018). Upon activation of SBE at 450°C, 500°C and 550°C (ASBE1, ASBE2 and ASBE3), the peaks shifted slightly to the left, causing an increase in the $d_{spacing}$ to approximately 3.37 Å, 3.368 Å, and 3.371 Å, respectively. Interestingly, the activation temperatures did not seem to significantly affect the $d_{spacing}$ of activated SBE.

The lattice spacing of ZnO calculated from ZnO peak at 2θ = 36.2141° was measured to be 2.4785 Å. Once ZnO was composited with SBE, the peaks slightly shifted to the left, and the $d_{spacings}$ of ZnO in KSBE1, KSBE2 and KSBE3 slightly increased to 2.62 Å, 2.49 Å and 2.48 Å, respectively. Meanwhile, the $d_{spacings}$ of SBE were calculated from the highest peak of SBE at 2θ ~ 26.4° in KSBE1, KSBE2, and KSBE3, resulting in values of 3.368 Å, 3.37 Å and 3.36 Å, respectively.

As SBE belongs to the family of montmorillonite clays, it can undergo intercalation, similar to other members of this group. Intercalation involves the insertion of certain species through cation exchange in the interlayer of the clay, thereby preserving its layered structure. This process results in an increased basal spacing within the clay. Upon heating, the layered structure transforms into a thermally stable mesoporous and/or microporous material, all the while retaining its original layer structure. This modified form of montmorillonite is commonly referred to as "pillared montmorillonite" (Al Kasour *et al*., 2022).

Prior studies on ZnO nanocomposites with montmorillonite reported that introducing ZnO into the clay resulted in a noticeable shift in the X-ray diffraction (XRD) peak of montmorillonite towards a lower angle. Furthermore, this incorporation of ZnO caused an increase in the $d_{spacing}$ of montmorillonite from 0.99 - 1.19 nm (Sani *et al*., 2017). In contrast, our research suggests that the compositing process of ZnO with SBE did not follow the typical pillaring or intercalating process. This conclusion is based on the observation that the $d_{spacings}$ of ZnO and SBE after the compositing process did not exhibit significant changes compared to their respective values before the process. Indeed, it is likely that the bonding mechanisms involved are of a low physical or mechanical nature. This suggests that the interaction between SBE and ZnO might not involve strong chemical bonds or substantial structural alterations. Instead, the compositing process may rely on weaker physical forces such as Van der Waals interactions or mechanical mixing.

Figure 2 displays the FTIR diagrams of the samples, namely pure SBE, pyrolysed SBE at 450°C (ASBE1), 500°C (ASBE2), and 550°C (ASBE3), as well as composite ZnO/SBE at 450°C (KSBE1), ZnO/SBE at 500°C (KSBE2), and ZnO/SBE at 550°C (KSBE3). FTIR analysis was employed to identify the chemical functional groups present in these samples and characterise their compositions. Pure SBE and activated SBE (*Figure 1a*) exhibit characteristic peaks corresponding to the –OH functional group at a wavelength of 3392 cm^{-1} (Majid and Mat, 2017). Additionally, peaks corresponding to Si-O functional groups are observed in the wavelength range of 420-485 cm^{-1}, Si-O-Si functional groups at 1017 cm^{-1}, and a C=C bond at 1636 cm^{-1}. Notably, no significant changes in the functional groups of SBE materials are observed before or after the activation process, even with temperature variations of 450°C, 500°C, and 550°C (Yulikasari *et al*., 2022), as evident from the FTIR results above. Furthermore, *Figure 1b* reveals additional peaks in the activated SBE samples, including –OH functional groups at wavelengths of 3277 cm^{-1} and 1408 cm^{-1}, a C=O functional group at 1637 cm^{-1} and a Zn-O functional group at 300-650 cm^{-1} (Hernández *et al*., 2007).

SEM characterisations were conducted on pure SBE, ASBE1, ASBE2, ASBE3, ZnO, KSBE1, KSBE2 and KSBE3 samples. As depicted in *Figure 3a*, the surface morphology of SBE exhibits a porous structure with montmorillonite phases, displaying irregular and nearly spherical shapes with sizes ranging from ~5-40 μm. *Figure 3b-3c* illustrate the surfaces of ASBE1, ASBE2 and ASBE3 samples, which exhibit increased pore openness as a result of the activation process with KOH and pyrolysis at high temperatures. *Figure 3e-3h* depict the surface morphologies of ZnO, KSBE1, KSBE2 and KSBE3. In *Figure 3e*, white lumps on the surface indicate the formation of ZnO. Meanwhile, in *Figure 3f-3g*, the presence of white lumps of ZnO on the surface of ASBE samples partially obstructs the pores of ASBE.

The elemental compositions of the samples, as shown in *Table 2* and *Figure 4a-4d*, were determined by EDX analysis. The main constituent elements of SBE were found to be Silicon (Si) at 38.54%, Oxygen (O) at 49.03% and Carbon (C) at 7.97%. Among the activated SBE samples, ASBE1, ASBE2 and ASBE3, oxygen had the highest composition with levels of 54.73%, 53.5% and 53%, respectively. Moreover, an increase in carbon content was observed with increasing temperature during the activation process, from 7.97% in pure SBE to 16.52% in ASBE activated at 500°C. Notably, the activated SBE at 500°C exhibited the highest carbon content compared to pure SBE and ASBE activated at 450°C and 550°C, respectively.

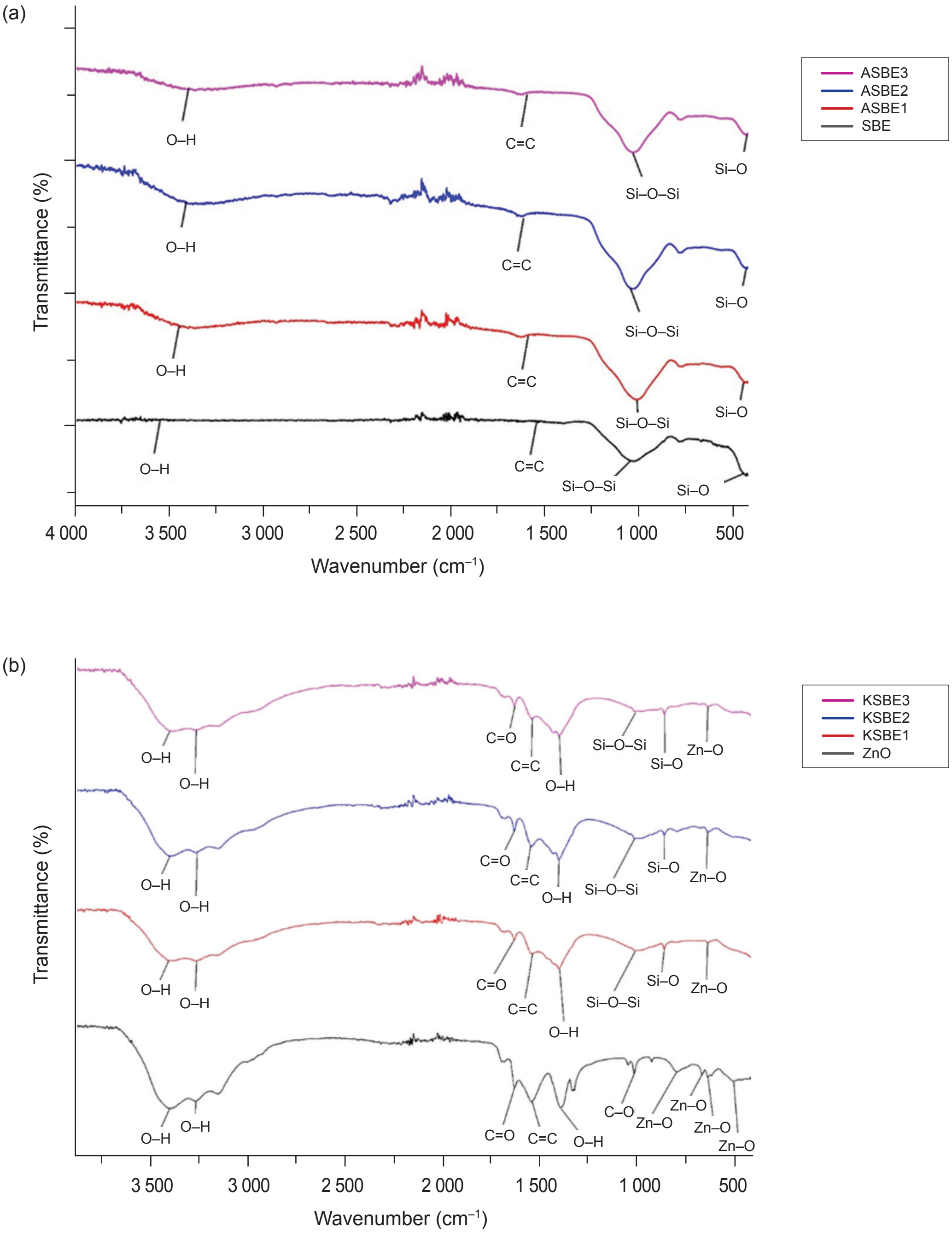

Figure 2. FTIR results of (a) SBE, ASBE1, ASBE2 and ASBE3, (b) ZnO, KSBE1, KSBE2 and KSBE3.

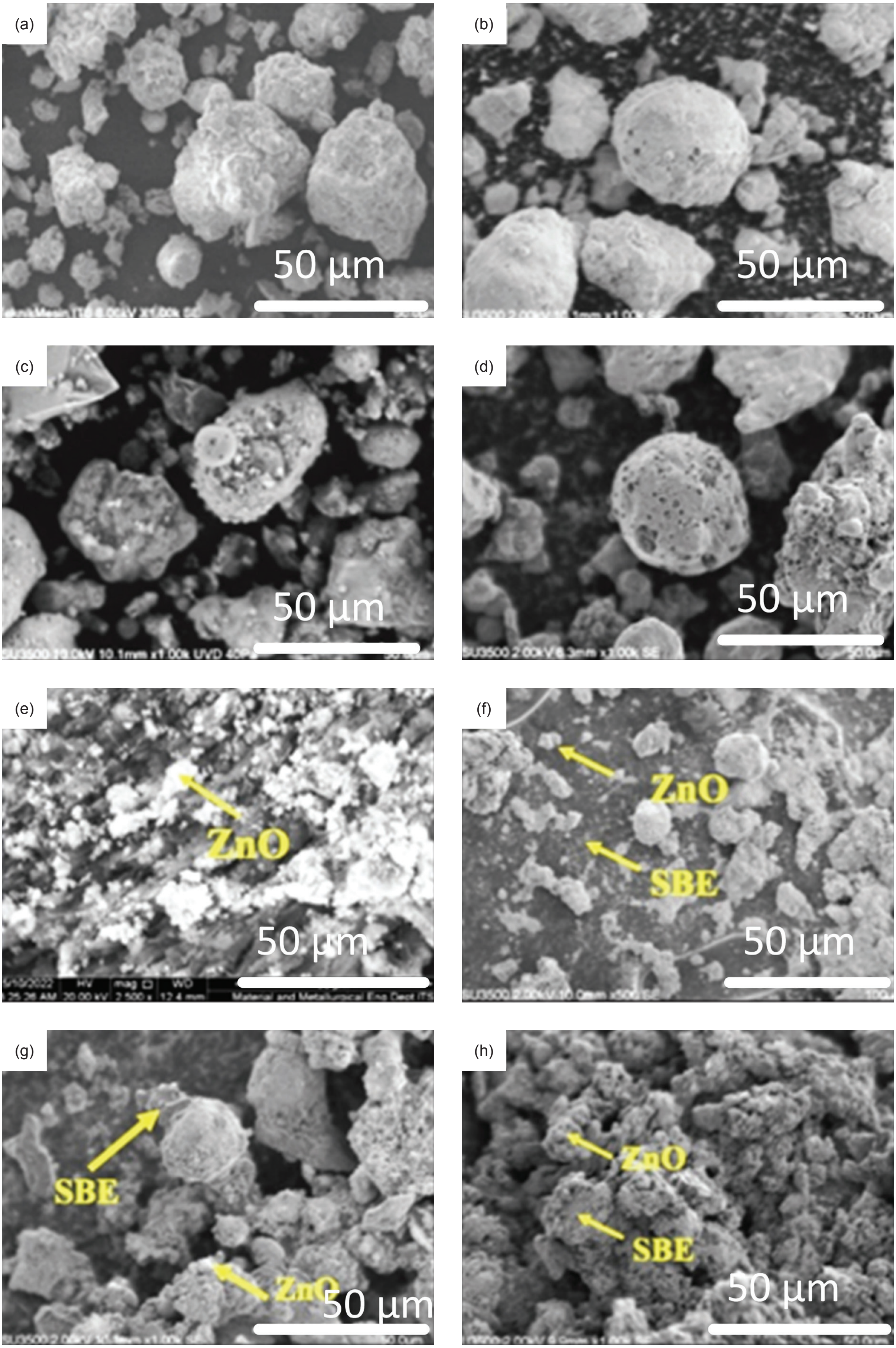

Figure 3. Bright Field Secondary Electron SEM images of (a) SBE, (b) ASBE1, (c) ASBE2, (d) ASBE3, (e) ZnO, (f) KSBE1, (g) KSBE2 and (h) KSBE3.

Table 2 and *Figure 4e-4h* also reveal that Zinc (Zn) was the major constituent element in ZnO and ZnO/SBE composite samples, with percentages of 43.30%, 44.06%, and 40.06% for KSBE1, KSBE2 and KSBE3, respectively. Additionally, the activated ZnO/SBE composite samples exhibited increased carbon content, similar to the activated SBE (ASBE) samples in *Table 2*. The highest carbon content of 21.68% was observed in the ZnO/SBE composite activated at 500°C. This carbon content originated from the remaining CPO in the SBE, which was thermally degraded during the pyrolysis process and formed 'biochar' (Foong *et al.*, 2022). Overall, these results were consistent with the XRD and FTIR findings, confirming the elemental composition of SBE as Si, O, and C.

The active surface area and pore total volume of pure SBE before and after activation at different temperatures (450°C for ASBE1, 500°C for ASBE2 and 550°C for ASBE3) were measured using the BET (Brunauer-Emmett-Teller) instrument. The tabulated results are provided in *Table 3*.

Table 3 shows that SBE, ASBE1, ASBE2, and ASBE3 have pore volumes of 0.038, 0.051, 0.119 and 0.098 $cm^3\ g^{-1}$, respectively. It is evident that there is an increase in pore volume for SBE after activation. However, when the activation temperature was set at 550°C, the pore volume decreased. This trend is also supported by the surface area measurements of SBE, ASBE1, ASBE2 and ASBE3. The surface area of SBE increased from 11.217 $m^2\ g^{-1}$ to 20.313 $m^2\ g^{-1}$ and 106.851 $m^2\ g^{-1}$ when activated at temperatures of 450°C and 500°C, respectively. However, when the pyrolysis temperature was set at 550°C, the surface area decreased to 74.600 $m^2\ g^{-1}$. The average pore diameters were 13.819 nm before the activation process, 5.048, 2.237 and 2.636 nm after activation at 450°C, 500°C and 550°C, respectively. Therefore, the SBE activated at 500°C exhibited the highest active surface area and total volume of pores due to the lowest average pore diameter. It is worth mentioning that the active surface area was not solely contributed by SBE, but also by the remaining carbon, which transformed into activated carbon, as confirmed by FTIR and EDX results. At higher temperatures, the functional groups of carbon were decomposed, resulting in a decrease in carbon content according to the EDX results, and consequently, a reduction in active surface area as well (Bazan *et al.*, 2016)

According to Rizkiyah *et al.* (2022), the active surface areas of SBE were reported as 88.7, 158.7 and 124.5 $m^2\ g^{-1}$ when activated at 400°C, 500°C, and 600°C, respectively. Similarly, Wafti *et al.* (2011) reported the active surface areas of SBE as 186, 206 and 72 $m^2\ g^{-1}$ when activated at 400°C, 500°C, and 800°C, respectively. These studies revealed that there is a turning point temperature where the maximum active surface area is achieved, and beyond this temperature, the active surface area reduces due to the decomposition of the activated carbon, which contributes to the formation of new pores. This finding is also supported by the XRD measurements of crystallite size, where smaller crystallite size corresponds to larger active surface area (Hossain *et al.*, 2018).

TABLE 2. THE ELEMENTAL COMPOSITIONS OF SBE, ASBE1, ASBE2, ASBE3, ZnO, KSBE1, KSBE2, KSBE3 BASED ON EDX MEASUREMENTS

No.	Sample	Wt (%)			
		Zn	Si	C	O
1	SBE	-	38.54	7.97	53.03
2	ASBE1	-	32.51	12.43	54.73
3	ASBE2	-	29.53	16.51	53.50
4	ASBE3	-	30.48	16.06	53.00
5	ZnO	63.96	-	-	36.04
6	KSBE1	43.30	7.89	12.23	36.58
7	KSBE2	44.06	3.68	21.68	30.58
8	KSBE3	40.06	6.69	20.80	31.55

TABLE 3. BET AND VOLATILE MATTER RESULTS OF SBE, ASBE1, ASBE2, ASBE3

No.	Sample	Active surface area ($m^2\ g^{-1}$)	Total volume of pores ($cm^3\ g^{-1}$)	Average pore diameter (nm)	Volatile matter (%)
1	SBE	11.217	0.038	13.819	-
2	ASBE1	20.313	0.051	5.048	6.14
3	ASBE2	106.851	0.119	2.237	3.54
4	ASBE3	74.600	0.098	2.636	4.02

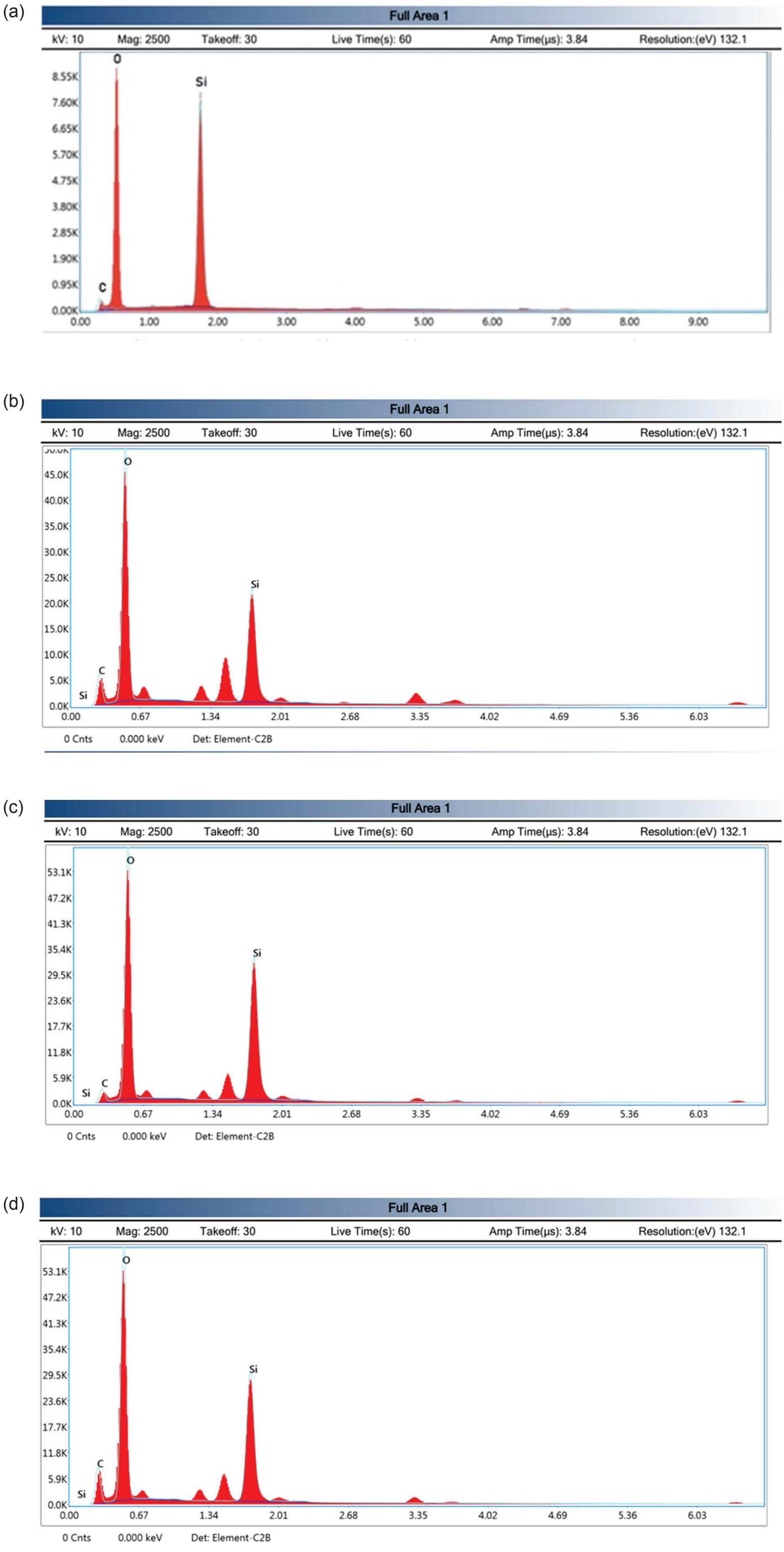
(a)
Full Area 1
kV: 10 Mag: 2500 Takeoff: 30 Live Time(s): 60 Amp Time(µs): 3.84 Resolution:(eV) 132.1
O
Si
C
8.55K
7.60K
6.65K
5.70K
4.75K
3.80K
2.85K
1.90K
0.95K
0.00K
0.00
1.00
2.00
3.00
4.00
5.00
6.00
7.00
8.00
9.00
(b)
Full Area 1
kV: 10 Mag: 2500 Takeoff: 30 Live Time(s): 60 Amp Time(µs): 3.84 Resolution:(eV) 132.1
O
Si
C
Si
45.0K
40.0K
35.0K
30.0K
25.0K
20.0K
15.0K
10.0K
5.0K
0.0K
0.00
0.67
1.34
2.01
2.68
3.35
4.02
4.69
5.36
6.03
0 Cnts 0.000 keV Det: Element-C2B
(c)
Full Area 1
kV: 10 Mag: 2500 Takeoff: 30 Live Time(s): 60 Amp Time(µs): 3.84 Resolution:(eV) 132.1
O
Si
C
Si
53.1K
47.2K
41.3K
35.4K
29.5K
23.6K
17.7K
11.8K
5.9K
0.0K
0.00
0.67
1.34
2.01
2.68
3.35
4.02
4.69
5.36
6.03
0 Cnts 0.000 keV Det: Element-C2B
(d)
Full Area 1
kV: 10 Mag: 2500 Takeoff: 30 Live Time(s): 60 Amp Time(µs): 3.84 Resolution:(eV) 132.1
O
Si
C
Si
53.1K
47.2K
41.3K
35.4K
29.5K
23.6K
17.7K
11.8K
5.9K
0.0K
0.00
0.67
1.34
2.01
2.68
3.35
4.02
4.69
5.36
6.03
0 Cnts 0.000 keV Det: Element-C2B

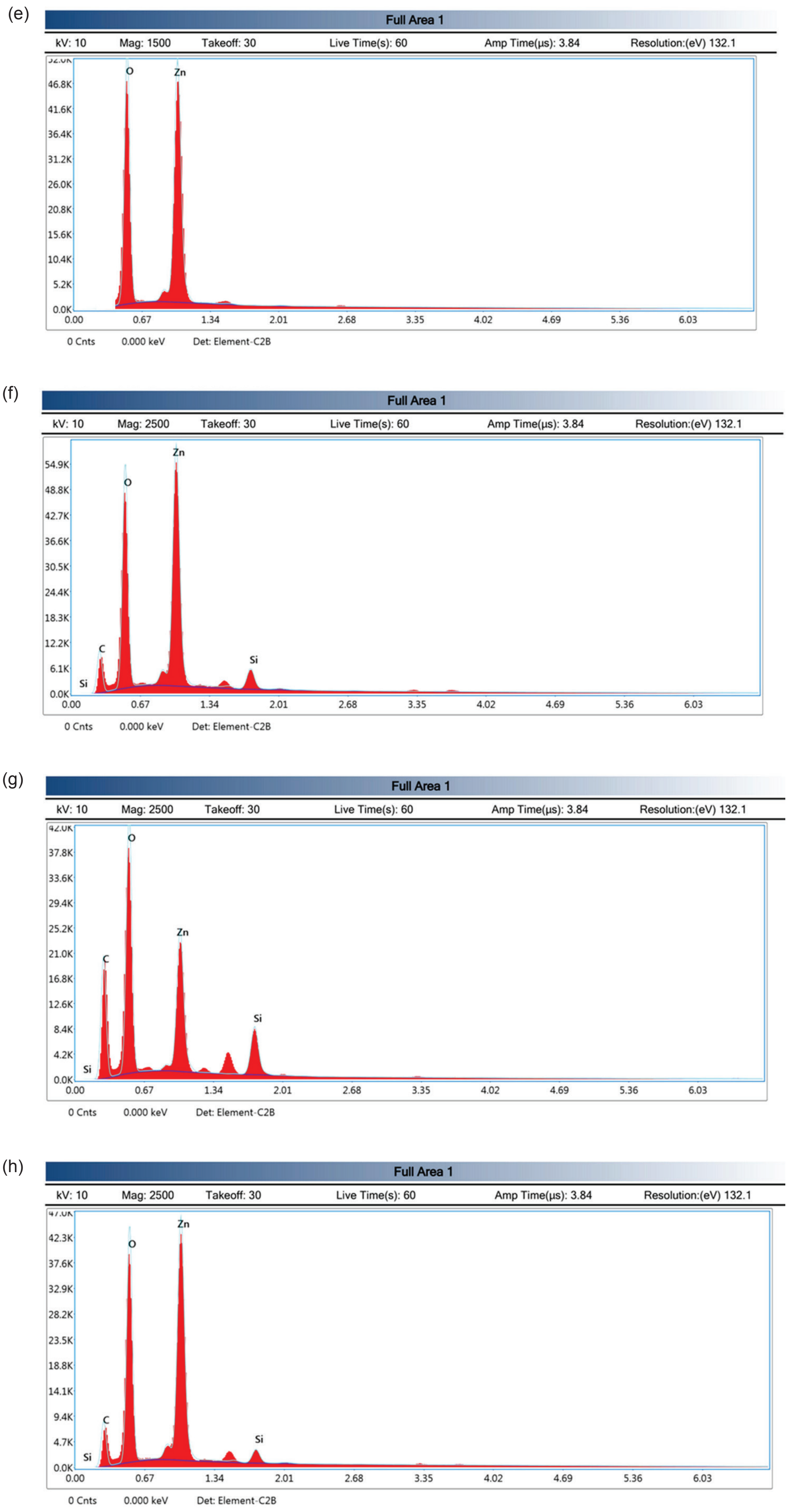

Figure 4. EDX analysis of (a) SBE, (b) ASBE1, (c) ASBE2, (d) ASBE3 (e) ZnO, (f) KSBE1, (g) KSBE2 and (h) KSBE3.

Similar findings were reported by Liu *et al.* (2021), where a decrease in surface area and pore volume was observed at higher activation temperatures. This decrease in surface area was attributed to pore damage caused by excessively high activation temperatures. On the other hand, the increase in surface area of SBE was generally attributed to the decomposition of organic matter and the release of volatile components during the activation process.

Furthermore, research has shown that the amount of carbon formed during the activation process is directly correlated with the pore volume and surface area of SBE. Additionally, pre-soaking of SBE with KOH prior to the activation process has been found to increase the surface area and adsorption capacity of SBE, as reported in previous research (Liu *et al.*, 2021).

Table 3 also presents the percentage of volatile matter for ASBE1, SBE2, and ASBE3 as 6.14%, 3.54% and 4.02%, respectively. Research conducted by Kusdarini *et al.* (2017) indicated that if the activation temperature increased, the percentage of volatile matter would decrease. This is because non-carbon compounds do not decompose during the activation process, resulting in less volatile matter being released. Furthermore, an increase in the number of pores formed due to the released volatile matter results in a decrease in the material's surface area. Based on the BET test results shown in *Table 3*, the ASBE2 sample has the largest surface area and corresponds to the percentage of low volatile matter.

Figure 5 displays the adsorption-desorption isotherm curves obtained from BET measurements of the samples plotted as volume adsorbed (STP cm^3 g^{-1}) *vs.* relative pressure (P/P_0). *Figure 5a* shows the curve of SBE which fits to type III adsorption isotherm classified by IUPAC. According to IUPAC, type III represents the nonporous or macro porous adsorbents (Zhang *et al.*, 2020). As classified by IUPAC, macroporous materials have pores with diameter > 50 nm, mesoporous materials have pores with diameter between 2-50 nm, while microporous materials have pores with diameter ≤ 2 nm (Alothman, 2012). However, referring to *Table 3*, the average pore diameter of SBE is 13.819 nm, indicating that SBE is a mesoporous material. The isotherm curve had a shape similar to that of type III, likely due to the presence of remaining CPO that covered the pores. This explanation is further supported by the desorption curve in *Figure 5a*, which was lower than the adsorption curve at $P/P_0 \leq 0.4$ (low pressure). It is possible that the sample was not degassed sufficiently, and some impurities may still be present.

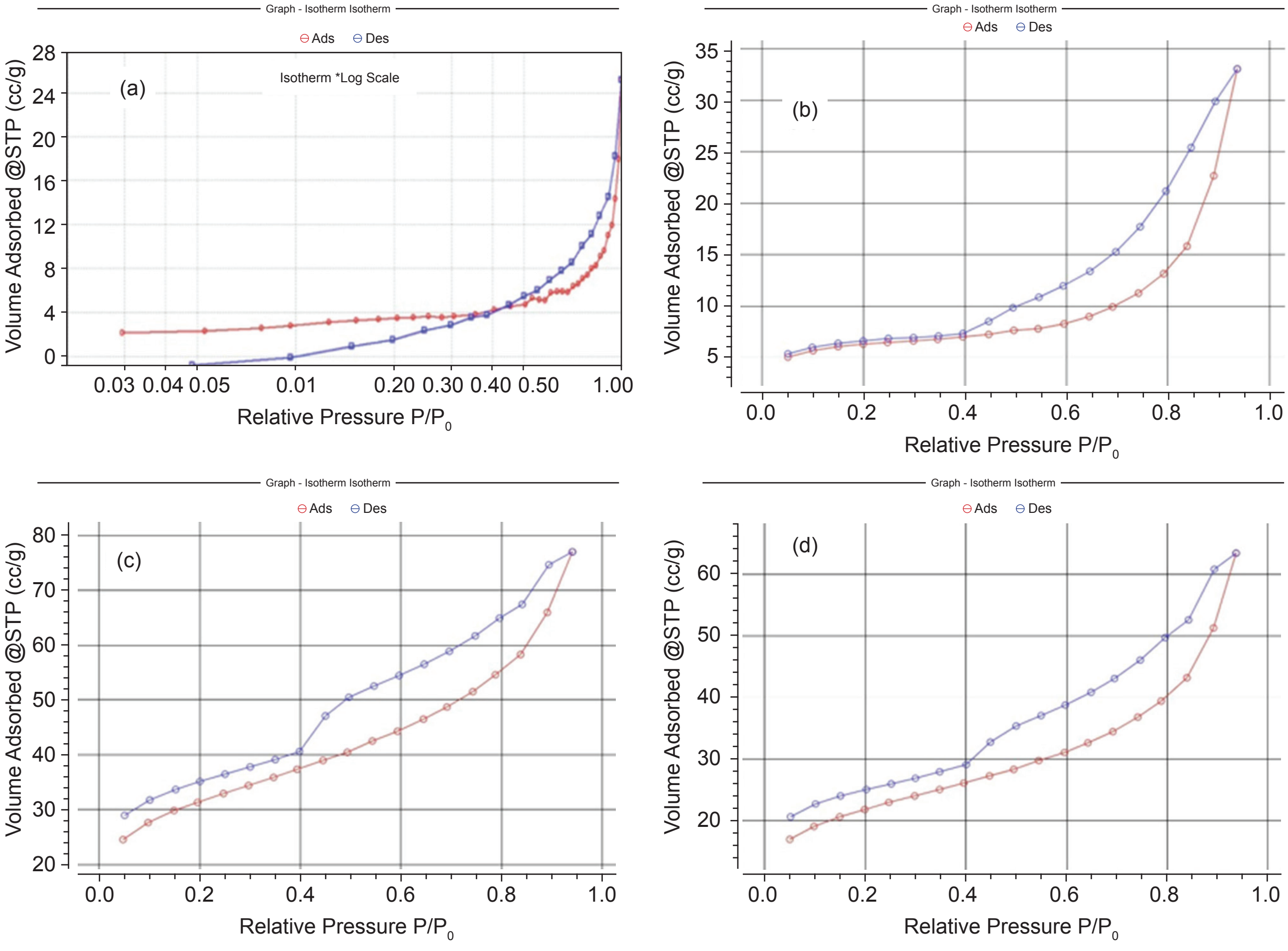

Figure 5. Adsorption-desorption curves from BET measurements (a) SBE, (b) ASBE1, (c) ASBE2, and (d) ASBE3.

Figure 5b appears to be a transition from *Figure 5a-5c*, because the desorption curve was only slightly higher than the adsorption curve. Therefore, the temperature of 500°C was likely not sufficient to activate the SBE. Additionally, the active surface area and the total volume of pores of ASBE1 were not significantly different from those of SBE, as shown in *Table 3*.

Figure 5b-5d exhibit adsorption-desorption hysteresis of type H_3, as classified by IUPAC. The three basic models of pores include cylindrical, ink-bottle, and slit-shape pores. Type H_3 represents the slit-shaped pores formed by non-rigid aggregates of plate-like particles (Alothman, 2012). Thus, the activated SBE samples had slit-shaped pores and were classified as mesoporous materials, with pore diameters ranging from 2.237 to 5.048 nm.

Figure 5 illustrates that the volume adsorbed of SBE (y axis) was the lowest, followed by ASBE1, ASBE3, and ASBE2. This trend is consistent with the results presented in *Table 3*, where ASBE2 had the smallest average pore diameter size and highest active surface area and total pore volumes, while SBE had the largest average pore diameter size and lowest active surface area and total pore volumes.

Figure 6a illustrates the UV-Vis measurement of RhB with a concentration of 12 ppm before undergoing photocatalysis. The maximum wavelength was observed at approximately 554 nm with an absorbance of around 2. This outcome served as the baseline to determine the absorbances of other concentrations in *Figure 6b*, which were then used to establish a standard for assessing changes in RhB concentration during the photocatalytic test based on UV-Vis absorbance.

In *Figure 6b*, RhB was subjected to varying concentrations of 2, 4, 6, 8, 10 and 12 ppm, yielding absorbance values of 0.295, 0.591, 1.104, 1.454, and 1.872, respectively. The resulting linear regression equation is $y = 0.1861x–0.0731$, where y denotes the absorbance of the solution, and x represents the concentration of the RhB solution (ppm). The coefficient of correlation (R^2) is equal to 0.98847, which indicates a strong linear relationship between concentration and absorbance based on the Lambert-Beer law, since the R^2 value approaches 1.

The results of UV-Vis measurements on the ZnO, SBE, KSBE1, KSBE2 and KSBE3 samples are presented in *Figure 6c* as absorbance *vs.* time of the photocatalytic experiments. Based on *Figure 6b*, these results were then converted into % degradation of RhB *vs.* time of the photocatalytic experiments,

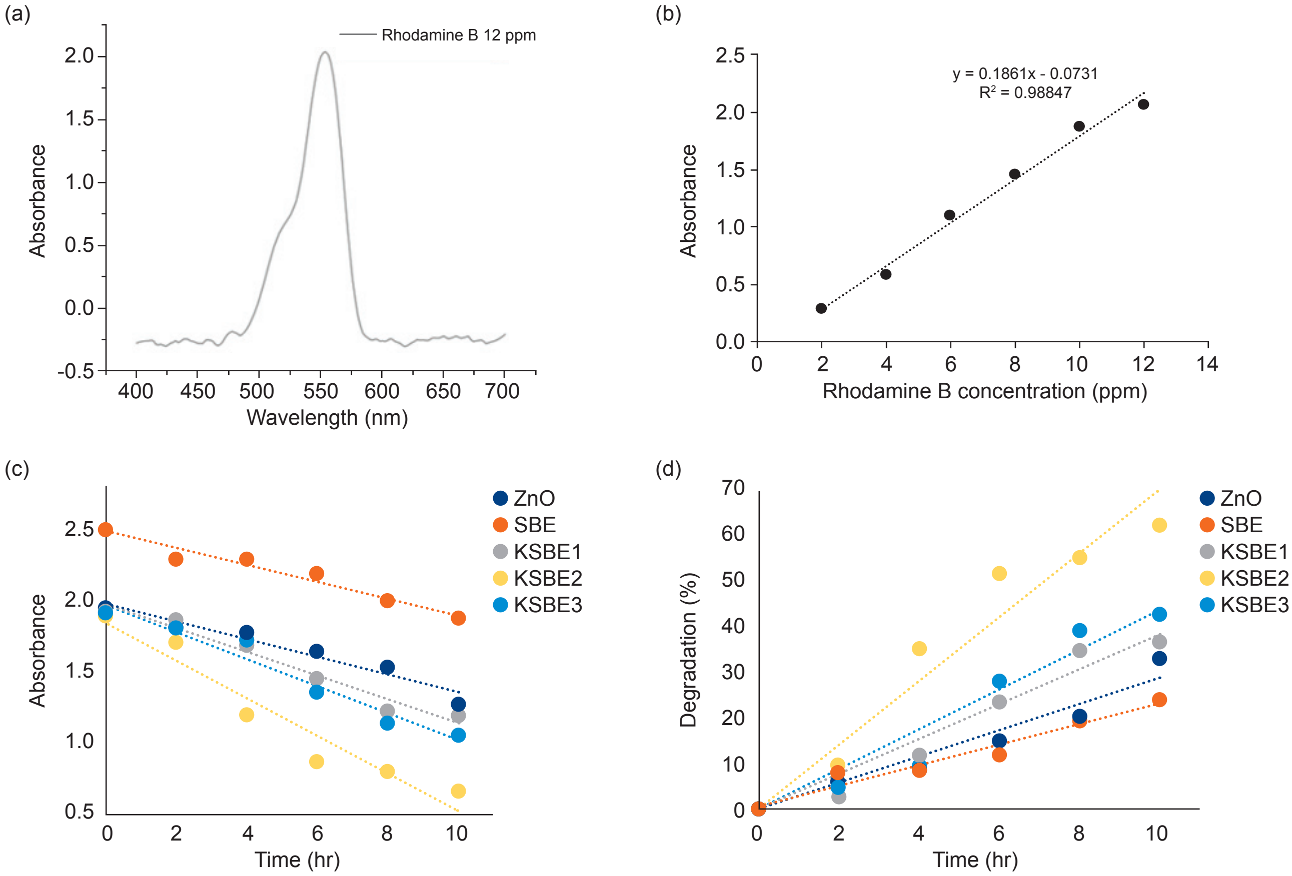

Figure 6. (a) UV-Vis measurement result of RhB 12 ppm. (b) Linear regression of UV-Vis measurement of RhB at concentrations of 2, 4, 6, 8, 10, and 12 ppm plotted as absorbance vs. *RhB concentration. (c) UV-Vis measurements on the ZnO, SBE, KSBE1, KSBE2, and KSBE3 samples. (d) The conversion of RhB UV-Vis measurements in* Figure 6c *into % degradation of ZnO, SBE, ASBE1, ASBE2 and ASBE3 samples.*

as shown in *Figure 6d*. After 10 hr of photocatalytic testing, KSBE2 showed the highest percentage degradation of RhB (62.5%), followed by KSBE3 (42.8%), KSBE1 (36.5%), ZnO (33.2%) and SBE (24%). Hence, drawing upon the aforementioned results and focusing on the most significant outcome, if we were to assess the contribution of SBE adsorption within the composite, an approximate estimation would be at 26.2%.

The percentage degradation results were consistent with the active surface area, with KSBE2 having the highest active surface area, followed by KSBE3, KSBE1, and SBE. The high active surface area allowed more RhB to be stored in the pore volume, resulting in an increased photo-degradation process. The compositing process of ZnO with SBE significantly improved the ability of ZnO as a photocatalyst semiconductor to degrade RhB. Moreover, if the trendline of KSBE2 in *Figure 6d* is extended to reach 100% degradation, the photocatalytic process will need approximately 14.3 hr to complete.

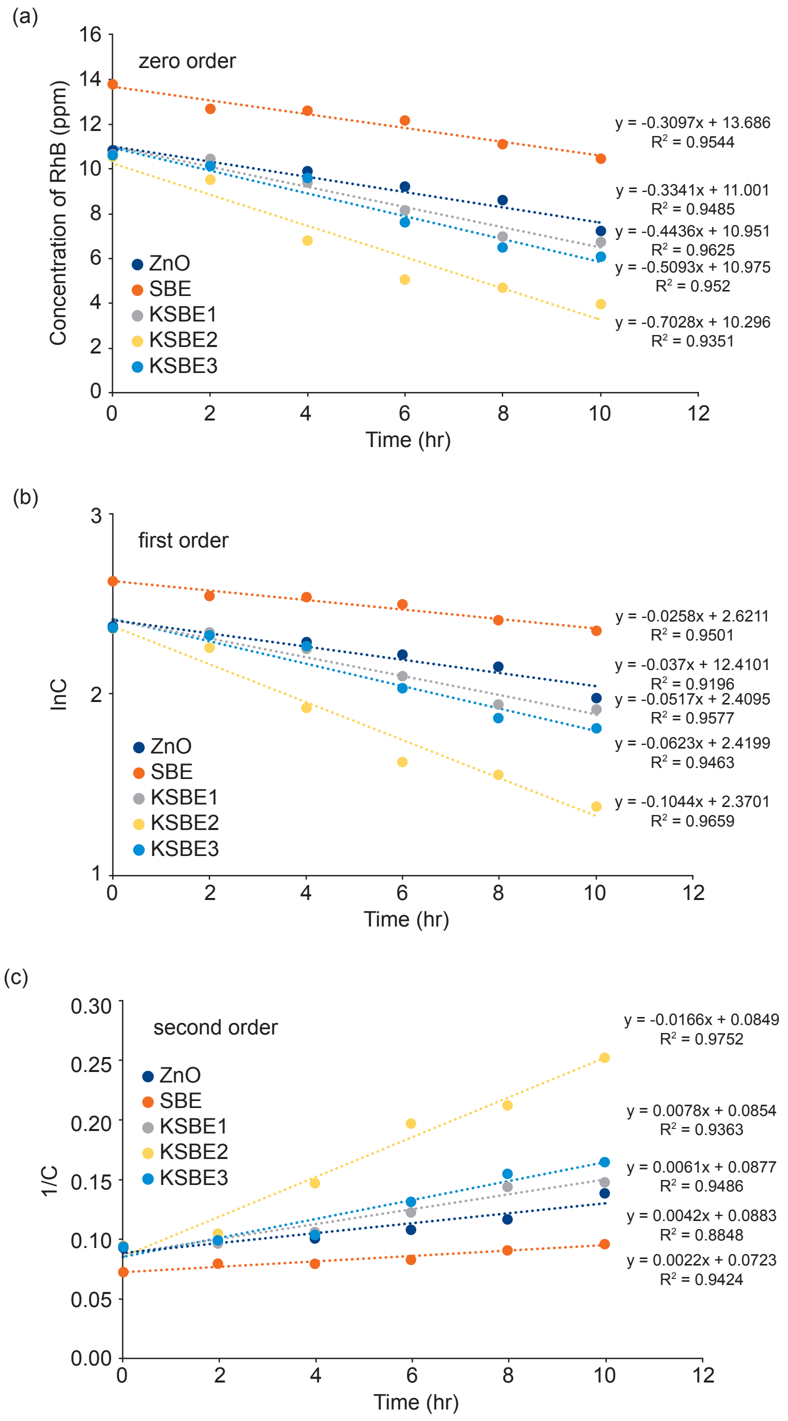

Figure 7. (a) Plot of RhB concentration (C) vs. *times follows zero order reaction, (b) plot of lnC* vs. *times follows first order reaction, and (c) plot of 1/C* vs. *times follows second order reaction to determine the pollutant degradation kinetic.*

Figure 7 displays linear plots of reaction rates for all samples to study the pollutant degradation kinetics. Zero order reaction rate can be expressed as follows (Upadhyaya and Dube, 1985):

$$\frac{dC}{dt} = -k \tag{4}$$

$$C = -kt + C_0 \tag{5}$$

where, C_0 is RhB concentration (ppm) at $t = 0$, C is RhB concentration (ppm) at any time, t (hr) and k (ppm hr^{-1}) is the reaction rate constant. After integration with initial value of $C = C_0$ at $t = 0$ and final value of $C = C$ at $t = t$, Equation (4) becomes Equation (5). Equation (5) was plotted as seen in *Figure 7a*.

For the first order reaction, the reaction rate can be expressed as follows (Upadhyaya and Dube, 1985):

$$\frac{dC}{dt} = -kC \tag{6}$$

Integration of Equation (6) results in Equation (7):

$$lnC = -kt + lncC_0 \tag{7}$$

And for the second order reaction, the reaction rate can be expressed as follows:

$$\frac{dC}{dt} = -kC^2 \tag{8}$$

In the same way, integration of Equation (8) results in Equation (9) (Upadhyaya and Dube, 1985):

$$\frac{1}{C} = kt + \frac{1}{C_0} \tag{9}$$

Equation (7) and (9) were linearly plotted in *Figure 7b* and *7c*, respectively.

The reaction rate constants (k) and the correlation coefficients (R^2) are listed in *Table 4*, as follows:

Notably, all experimental data exhibit a strong correlation with linear trendlines, boasting correlation coefficients (R^2) exceeding 93.51% for zero order reaction kinetic, 91.96% for first order reaction kinetic and 88.48% for second order reaction kinetic. Consequently, it can be inferred that the degradation kinetics of RhB adhere to the zero-order reaction model. The reaction rate constants ranked from the highest to lowest for all the kinetic models were as follows: KSBE2, KSBE3, KSBE1, ZnO, and SBE. Hence the reaction rates ranked from the fastest to the slowest were KSBE2, KSBE3, KSBE1, ZnO, and SBE.

The results of RhB degradation in *Figure 6d* were probably less than reported in other papers. For example, Slamet *et al*. (2021) conducted a study comparing the adsorption ability of SBE/ZnO composite towards RhB waste in both dark and ambient light conditions. The results revealed that the presence of ambient light significantly enhanced the adsorption ability, reaching up to 147.059 mg g^{-1}. In a study by Rahayu and Nurhayati (2023), the abilities of SBE and activated SBE to adsorb RhB dye were compared. The highest removal efficiency reported was 76.77% for SBE and 81.8% for activated SBE. The adsorption kinetics followed a pseudo-second order reaction.

In another study conducted by Yulikasari *et al.* (2023), a catalytic ozonation process using SBE/ZnO was employed to remove RhB. Remarkably, the RhB dye was removed by 97.43% within just 12 min, with a catalyst dose of 0.5 g L^{-1}, a pH of 7, and an ozone flow rate of 3 L min^{-1}. However, the methods of the reported research mentioned above were different from our research.

The ZnO/montmorillonite photocatalyst, as reported by Haounati *et al*. (2023), exhibited an impressive 99% maximum degradation efficiency of RhB after 70 min of UV light irradiation when there was no scavenger agent added to the RhB solution. The degradation followed a first-order reaction kinetic. In contrast, the TiO_2/montmorillonite composite studied by Djellabi *et al*. (2014) achieved a degradation efficiency of 79.8% for RhB under UV-A irradiation over a longer duration of 6 hr. It is worth noting that both

TABLE 4. COMPARISON OF ZERO ORDER, FIRST ORDER, AND SECOND ORDER RHB DEGRADATION KINETICS PARAMETERS

Sample	Zero order		First order		Second order	
	k (ppm hr^{-1})	R^2	k (ppm hr^{-1})	R^2	k (ppm hr^{-1})	R^2
ZnO	0.3341	0.9544	0.037	0.9196	0.0042	0.8848
SBE	0.3097	0.9485	0.0258	0.9501	0.0022	0.9424
KSBE1	0.4436	0.9625	0.0517	0.9577	0.0061	0.9486
KSBE2	0.7028	0.952	0.1044	0.9659	0.0166	0.9752
KSBE3	0.5093	0.9351	0.0623	0.9463	0.0078	0.9363

studies involved photocatalyst composites using fresh montmorillonite, unlike SBE, which utilises spent montmorillonite.

Hindryawati *et al.* (2020) reported the degradation of 99.12% of methylene blue (MB) by SBE impregnated with WO_3 catalyst during 2 hr of photocatalytic experiment and Saputra *et al.* (2020) reported the degradation of 99.5% of MB by $CeFeO_3$/calcinated SBE after 2 hr photocatalytic test. The experiment conducted by Pinto *et al.* (2019) reported the RhB degradation of maximum 80.46% after 24 hr photocatalytic contact using geopolymer material. Hence, research of ZnO/SBE as a photocatalyst for photodegradation of RhB is still rarely found, so comparison of the same photocatalyst material and solution waste was difficult to find.

SBE, a type of montmorillonite clay, is categorised as an insulator material. The electrical conductivity of montmorillonite shows temperature dependence; at 100°C, it ranges from 7.94×10^{-13} to 1.58×10^{-9} Ω^{-1} cm^{-1}, while at 1000°C, it ranges from 5.01×10^{-6} to 8.71×10^{-4} Ω^{-1} cm^{-1}. The activation energy of montmorillonite's electrical conductivity is relatively low, ranging from 0.2 to 4.1 eV (Guseinov, 2017). Lower activation energy corresponds to a higher energy band gap, while higher activation energy indicates a smaller energy band gap (Sawicki *et al.*, 2016). Consequently, with its low activation energy of electrical conductivity, montmorillonite exhibits a relatively high energy band gap. Previous studies have reported the energy band gap of montmorillonite as 4.75 eV (Horwarth and Liang, 2011), 4.63 eV for Mg^{2+}-doped montmorillonite, and 4.3 eV for Fe^{2+}-doped montmorillonite (Ferreira *et al.*, 2019). These values further support the insulating properties of montmorillonite. On the other hand, ZnO is a semiconductor material with an energy band gap of 3.21 eV (Haounati *et al.*, 2023). Hence in this research, the photocatalytic activity was solely governed by ZnO without heterojunction mechanism of ZnO and SBE.

Figure 8 represents the schematic diagram of RhB photodegradation by composite of ZnO/SBE. Theoretically, when a photocatalyst semiconductor material such as ZnO is exposed to light energy, such as sunlight, its electrons (e^-) are excited from the valence band to the conduction band. This leaves holes (h^+) in the valence band which directly oxidise the pollutant (RhB). Additionally, the electrons (e^-) in the conduction band can react with oxygen to produce superoxide anion radicals $\bullet O_2^-$. The O_2^- can react with H_2O to form •OH radicals. These •OH and $\bullet O_2^-$ radicals then participate in redox reactions with organic compounds, such as RhB, causing the breakage of chemical bonds and the production of new compounds (Rajendrachari *et al.*, 2021) and (Irfan *et al.*, 2019).

Further explanation, the conduction band potential (E_{CB}) and valence band potential (E_{VB}) of ZnO, as determined by Haounati *et al.* (2023) using the Butler and Ginley method, were -0.32 eV and +2.88 eV *vs.* the normal hydrogen electrode

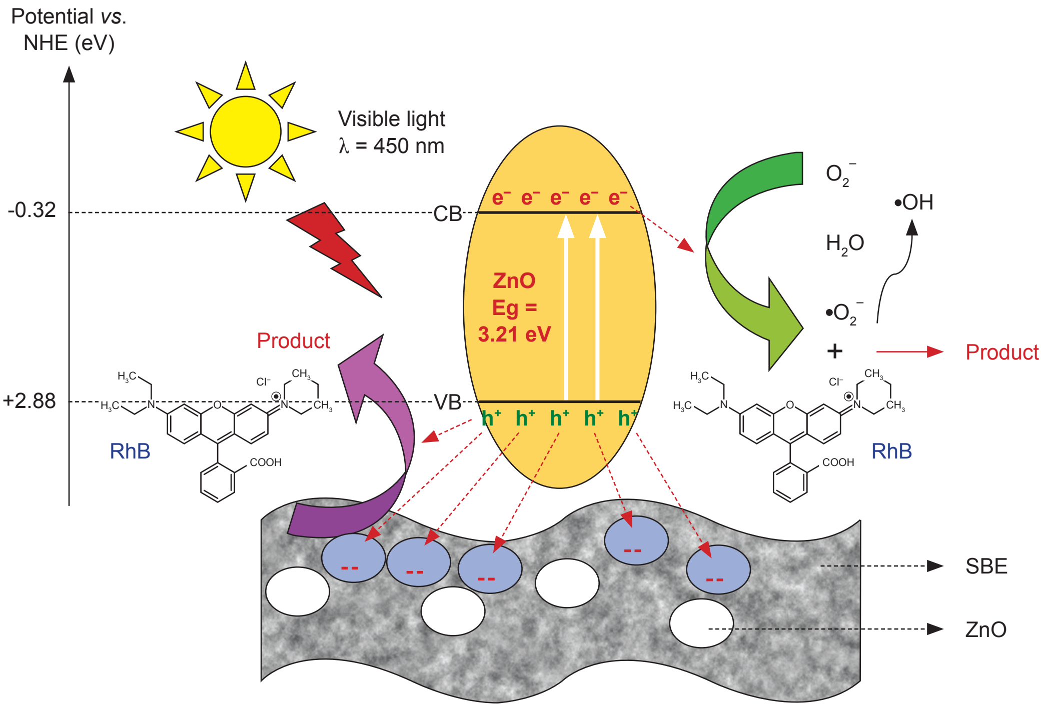

Figure 8. Schematic illustration of RhB photodegradation assisted by ZnO/SBE composite photocatalyst.

(NHE), respectively. Due to the E_{CB} potential of ZnO (-0.32 eV) being more positive than the reduction potential of O_2/O_2^- (-0.33 eV *vs.* NHE), the electrons are unable to reduce O_2 into O_2^-. Instead, the electrons in ZnO conduction band react with dissolved O_2 to produce H_2O_2, given that the potential of the electron is more negative than the reduction potential of O_2 to H_2O_2 (+0.682 eV *vs.* NHE). Furthermore, the produced H_2O_2 reacts with ZnO electrons in conduction band to generate •OH radicals and OH^- (Haounati *et al.*, 2023).

Meanwhile, the potential of the ZnO conduction band electrons is more negative than that of OH/H_2O (~2.72 eV *vs.* NHE), resulting in the inability of the holes to react with OH^- to produce •OH. Consequently, the holes directly react with RhB, degrading it through an oxidation reaction to form products such as CO_2 and H_2O.

The incorporation of SBE led to a homogeneous dispersion of ZnO species and the establishment of a well-connected interface between ZnO particles and SBE layers, facilitated by electrostatic interactions or weak physical bonds, such as Van der Waals forces, as previously observed in XRD results. Consequently, the excited electron-hole pairs of ZnO could efficiently migrate due to the electrostatic repulsion between the negatively charged electrons and the negatively charged SBE layers. In comparison to pure ZnO, the likelihood of electron-hole recombination in ZnO photocatalysts was substantially reduced, enabling more electrons to react with adsorbed O_2, thereby generating sufficient $•O_2^-$ and resulting in an improved photocatalytic activity (Li *et al.*, 2016). The enhanced adsorption of RhB and O_2 facilitated by the increased active surface area of SBE led to a higher percentage of RhB degradation. As a result, the sample KSBE2 exhibited the most significant degradation performance due to its highest active surface area among the tested samples.

The remaining RhB solution, with a molecular structure of $C_{28}H_{31}ClN_2O_3$ and a molecular weight of 479.017 g mol^{-1}, underwent Gas Chromatography-Mass Spectroscopy (GC-MS) analysis to determine if it had been degraded after photocatalytic test. The results, shown in *Table 5*, indicate that RhB was broken down into 6 new compounds, confirming the effectiveness of the photocatalytic process.

Figure 6d and *Table 5* provide evidence that the degradation of RhB resulted from both photocatalytic and adsorption mechanisms. If degradation were exclusively attributed to the photocatalytic process, one would anticipate the most substantial photodegradation percentage to appear in *Figure 6d*, corresponding to the ZnO photocatalyst material. Nevertheless, if the degradation were primarily prompted by the adsorption mechanism, the transformation of RhB into different materials, as outlined in *Table 5*, would not be observed.

These findings support the conclusion that the degradation of RhB involved a combination of both photocatalysis and adsorption processes.

CONCLUSION

Composites of ZnO and activated SBE have been successfully synthesised and used as photocatalyst materials for the photodegradation process of RhB through combination of two mechanisms, photocatalytic by ZnO and adsorption by activated SBE and follow zero order reaction kinetic. The pyrolysis process has proven to be effective in enhancing the properties of SBE, and a pyrolysis temperature of 500°C yielded the best photocatalytic result due to the superior structure and properties of the material, as indicated by the material characterisation measurements. Based on BET analysis, the surface area of SBE, ASBE1, ASBE2 and ASBE 3 were 11.217, 20.313, 106.851 and 74.6 m^2 g^{-1}, respectively. After 10 hr of photocatalytic testing, KSBE2 showed the highest % degradation of RhB (62.5%), followed by KSBE3 (42.8%), KSBE1 (36.5%), ZnO (33.2%), and SBE (24%). These results were certainly in line with the BET results. SBE facilitated the creation of a larger active area for the dispersion of ZnO, adsorption of RhB and O_2 and played a role in impeding the recombination of ZnO's electron-hole pairs through a repulsion mechanism between the negatively charged electrons and the negatively charged SBE surface. GC-MS analysis revealed that RhB was decomposed into six new compounds after the photocatalytic test. Thus, the photocatalyst material was effective in decomposing RhB, demonstrating its potential for

TABLE 5. GC-MS RESULTS OF RHB SOLUTION AFTER PHOTOCATALYTIC TEST

No.	Compound name	Chemical formula	Percentage (%)
1	9,12-Octadecadienoic acid	$C_{18}H_{32}O_2$	9.720
2	Methyl Octadetanoate	$C_{19}H_{38}O_2$	23.292
3	8-Octadecenoic acid, methyl ester	$C_{19}H_{36}O_2$	23.068
4	Octadecadienoic acid, methyl ester	$C_{19}H_{34}O_2$	23.019
5	Hexadecanoic acid, methyl ester	$C_{17}H_{34}O_2$	7.840
6	Methylbenzene	C_7H_8	4.140

environmental remediation applications despite of the lower degradation percentage compared to the other reported research.

ACKNOWLEDGEMENT

The authors would like to acknowledge the funding support provided by the Taiwan-Indonesia Science and Technology Innovation Centre for Circular Economy and Green Innovative Resources year 2022, under the National Taiwan University of Science and Technology (NTUST). The authors also acknowledge the research facilities provided by the Materials and Metallurgical Engineering Department, Institut Teknologi Sepuluh Nopember (ITS). The valuable support and contributions to this research project were sincerely appreciated.

REFERENCES

Alothman, Z A (2012). A review: Fundamental aspects of silicate mesoporous materials. *Materials*, *5(12)*: 2874-2902. DOI: 10.3390/MA5122874.

Al Kausor, M; Gupta, S S; Bhattacharyya, K G and Chakrabortty, D (2022). Montmorillonite and modified montmorillonite as adsorbents for removal of water soluble organic dyes: A review on current status of the art. *Inorg. Chem. Comm.*, *143(109686)*: 1-23. DOI: 10.1016/j.inoche.2022.109686.

Amritphale, S S; Mishra, D; Mudgal, M; Chouhan, R K and Chandra, N (2016). A novel green approach for making hybrid inorganic - organic geopolymeric cementitious material utilizing fly ash and rice husk. *J. Enviro. Chem. Eng.*, *4(4)*: 3856-3865. DOI: 10.1016/J.JECE.2016.08.015.

Aristanti, Y; Minandar, N; Marliani and Soepriyanto, S (2019). Analisis laju degradasi Rhodamine B (RhB) pada proses fotokatalisis TiO_2. *Ensains*, *2(3)*: 188-194.

Bahram, M; Talebi, R; Naseri, A and Nouri, S (2014). Modeling and optimization of removal of Rhodamine - B from wastewaters by adsorption on modified clay. *Chiang Mai J. Sci.*, *41(5.2)*: 1230-1240.

Bazan, A; Nowicki, P; Półrolniczak, P and Pietrzak, R (2016). Thermal analysis of activated carbon obtained from residue after supercritical extraction of hops. *J. Therm. Anal. Cal.*, *125(3)*: 1199-1204. DOI: 10.1007/S10973-016-5419-5/TABLES/4.

Cambrussi, A N C O; Morais, A Í S; Neris, A de M; Osajima, J A; Filho, E C da S and Ribeiro, A B (2019). Photodegradation study of TiO_2 and ZnO in suspension using miniaturized tests. *Revista Materia (Rio de Janeiro)*, *24(4)*. DOI: 10.1590/s1517-707620190004.0807.

Chen, Y; Yu, Y; Yan, Z; Li, T; Jing, Q and Liu, P (2022a). Montmorillonite induced assembly of multi-element doped g-C_3N_4 nanosheets with enhanced activity for Rhodamine B photodegradation. *Appl. Clay Sci.*, *218(106432)*: 1-12. DOI: 10.1016/j.clay.2022.106432

Chen, Y; Shi, Y; Wan, D; Zhao, J; He, Q and Liu, Y (2022b). Synergistic adsorption and advanced oxidation activated by persulfate for degradation of tetracycline hydrochloride using iron-modified spent bleaching earth carbon. *Enviro. Sci. Pollut. Res.*, *29(17)*: 24704-24715. DOI: 10.1007/S11356-021-17435-0/METRICS.

Cullity, B D and Stock, S R (2014). *Elements of X Ray Diffraction*. 3rd edition. Pearson Education Limited, England. p. 95 and 402.

Djellabi, R; Ghorab, M F; Cerrato, G; Morandi, S; Gatto, S; Oldani; V; Di Michele, A and Bianchi, C L (2014). Photoactive TiO_2-montmorillonite composite for degradation of organic dyes in water. *J. Photochem. Photobio. A: Chem.*, *295*: 57-63.

Dianggoni, I; Saputra, E and Pinem, J A (2017). Pengolahan zat warna tekstil (Rhodamine B) dengan teknologi AOP (advance oxidation processes) menggunakan katalis ce@carbon sphere dan oksidan *peroxymonosulfate*. *Jom Fteknik*, *4(2)*: 1-7.

Faramarzi, A H; Kaghazchi, T; Ebrahim, H A and Ebrahimi, A A (2015). Experimental investigation and mathematical modeling of physical activated carbon preparation from pistachio shell. *J. Anal. Appl. Pyrolysis*, *114*: 143-154. DOI: 10.1016/J.JAAP.2015.05.012.

Ferreira, C R; Pulcinelli, S H; Scolfaro, L and Borges, P D (2019). Structural and electronic properties of iron-doped sodium montmorillonite clays: A first-principles DFT study. *ACS Omega*, *4(11)*: 14369-14377. DOI: 10.1021/acsomega.9b00685.

Foong, S Y; Chan, Y H; Cheah, W Y; Kamaludin, N H; Ibrahim, T N B T; Sonne, C; Peng, W; Show, P L and Lam, S S (2021). Progress in waste valorization using advanced pyrolysis techniques for hydrogen and gaseous fuel production. *Biores. Tech.*, *320*: 124299. DOI: 10.1016/j.biortech.2020.124299.

Foong, S Y; Chan, Y H; Chin, B L F; Lock, S S M; Yee, C Y; Yiin, C L; Peng, W and Lam, S S (2022). Production of biochar from rice straw and its application for wastewater remediation - An overview. *Biores. Tech.*, *360(2)*: 127588. DOI: 10.1016/j.biortech.2022.127588.

Fu, J; Zhang, J; Jin, C; Wang, Z; Wang, T; Cheng, X and Ma, C (2020). Effects of temperature, oxygen and steam on pore structure characteristics of coconut husk activated carbon powders prepared by one-step rapid pyrolysis activation process. *Biores. Tech., 310*: 123413. DOI: 10.1016/J.BIORTECH.2020.123413.

Guseinov, A A (2017). Electrical properties of montmorillonite studied together with the processes occurring under thermal activation. *Izvestiya, Phys. Sol. Earth, 53*: 845-854. DOI: 10.1134/S1069351317060015.

Ha, T T; Canh, T D and Tuyen, N V (2013). A quick process for synthesis of ZnO nanoparticles with the aid of microwave irradiation. *Inter. Scho. Res. Not., 2013*: 1-8. DOI: 10.1155/2013/497873.

Haounati, R; Ighnih, H; Malekshah, R E; Alahiane, S; Alakhras, F; Alabbad, E; Alghamdi, H; Ouachtak, H; Addi, A A and Jada, A (2023). Exploring ZnO/montmorillonite photocatalysts for the removal of hazardous RhB Dye: A combined study using molecular dynamics simulations and experiments. *Mater. Today Comm., 35*: 105915. DOI: 10.1016/j.mtcomm.2023.105915.

Heriyanti; Prendika, W; Ashyar, R and Sutrisno (2018). Thermal behaviour and microanalysis of coal subbituminus. *IOP Conf. Series: Mater. Sci. Eng., 345(1)*: 012015. DOI: 10.1088/1757-899X/345/1/012015.

Hernández, A; Maya, L; Sánchez-Mora, E and Sánchez, E M (2007). Sol-gel synthesis, characterization and photocatalytic activity of mixed oxide ZnO-Fe_2O_3. *J. Sol-Gel Sci. Tech., 42(1)*: 71-78. DOI: 10.1007/S10971-006-1521-7/METRICS.

Hindryawati, N; Julia, R N D; Panggabean, A S and Wilsoma (2020). Ultrasound assisted the degradation of methylene blue using WO_3-deoiled spent bleaching earth as a catalyst. *IOP Conf. Series: Mater. Sci. Eng., 854(1)*: 012058. DOI: 10.1088/1757-899X/854/1/012058.

Horwath, W and Liang, Y L (2011). Variations of chemical composition and band gap energies in hectorite and montmorillonite clay minerals on sub-micron length scales. *Final Report. Kearney Foundation of Soil Science*. p. 1-62.

Hu, X and Gholizadeh, M (2019). Biomass pyrolysis: A review of the process development and challenges from initial researches up to the commercialisation stage. *J. Energy Chem., 39*: 109-143. DOI: 10.1016/J.JECHEM.2019.01.024.

Hossain, M K; Pervez, M F; Uddin, M J; Tayyaba, S; Mia, M N H; Bashar, M S; Jewel, M K H; Haque, M A S; Hakim, M A and Khan, M A (2018). Influence of natural dye adsorption on the structural, morphological and optical properties of TiO_2 based photoanode of dye-sensitized solar cell. *Mater. Sci. - Poland, 36(1)*: 93-101. DOI: 10.1515/MSP-2017-0090.

Ilmi, M M; Nurdini, N; Maryanti, E; Setiawan, P and Ismunandar, I (2021). X-ray diffraction peak profile for determination of microstructural properties of hematite (Fe_2O_3). *J. Res. Develop. Nanotech., 1(1)*: 11-17. DOI: 10.5614/JRDN.2021.1.1.16667.

Irfan, S; Zhuanghao, Z; Li, F; Chen, Y X; Liang, G X, Luo, J T and Ping, F (2019). Critical review: Bismuth ferrite as an emerging visible light active nanostructured photocatalyst. *J. Mater. Res. Tech., 8(6)*: 6375-6389. DOI: 10.1016/J.JMRT.2019.10.004.

Isnugroho, K; Birawidha, D C and Hendronursito, Y (2016). The biomass waste use as a secondary energy source for metal foundry process. *AIP Conf. Proc., 1746(1)*: 20001. DOI: 10.1063/1.4953926/1020418.

Kementerian Lingkungan Hidup dan Kehutanan Republik Indonesia (2020). Peraturan Menteri LHK Nomor 10 Tahun 2020, Alternatif Solusi KLHK untuk Pengelolaan Limbah B3 SBE - Kementerian LHK. https://www.menlhk.go.id/site/single_post/3003, accessed on 7 May 2023.

Khan, I; Saeed, K; Zekker, I; Zhang, B; Hendi, A H; Ahmad, A; Ahmad, S; Zada, N; Ahmad, H; Shah, L A; Shah, T and Khan, I (2022). Review on methylene blue: Its properties, uses, toxicity and photodegradation. *Water, 14(2):* 242. DOI: 10.3390/w14020242.

Kusdarini, E; Budianto, A and Ghafarunnisa, D (2017). Produksi karbon aktif dari batubara bituminus dengan aktivasi tunggal H_3PO_4, kombinasi H_3PO_4-NH_4HCO_3, dan termal. *Reaktor, 17(2)*: 74-80. DOI: 10.14710/REAKTOR.17.2.74-80.

Lee, C G; Seng, C E and Liew, K Y (2000). Solvent efficiency for oil extraction from spent bleaching clay. *J. Am. Oil Chem. Soc., 77(11)*: 1219-1223. DOI: 10.1007/S11746-000-0190-6.

Lesaoana, M; Mlaba, R P V; Mtunzi, F M; Klink, M J; Edijike, P and Pakade, V E (2019). Influence of inorganic acid modification on Cr(VI) adsorption performance and the physicochemical properties of activated carbon. *South Afr. J. Chem. Eng., 28*: 8-18. DOI: 10.1016/j.sajce.2019.01.001.

Li, C; Sun, Z; Huang, W and Zheng, S (2016). Facile synthesis of g-C_3N_4/montmorillonite composite with enhanced visible light photodegradation of rhodamine B and tetracycline. *J. Taiwan Inst. Chem. Eng.*, *66*: 363-371. DOI: 10.1016/j.jtice.2016.06.014.

Liu, W; Yuan, K; Yin, K; Zuo, S and Yao, C (2021). Clay-activated carbon adsorbent obtained by activation of spent bleaching earth and its application for removing Pb(II) ion. *Enviro. Sci. Pollut. Res.*, *28(1)*: 711-723. DOI: 10.1007/s11356-020-10473-0.

Mana, M; Ouali, M S; de Menorval, L C; Zajac, J J and Charnay, C (2011). Regeneration of spent bleaching earth by treatment with cethyltrimethylammonium bromide for application in elimination of acid dye. *Chem. Eng. J.*, *174(1)*: 275-280. DOI: 10.1016/J.CEJ.2011.09.026.

Majid, R A and Mat, C R C (2017). Regenerated spent bleaching earth for the decolourisation and BOD reduction of palm oil mill effluent. *J. Oil Palm Res.*, *29(4)*: 579-587. DOI: 10.21894/jopr.2017.0006.

Nurbayasari, R and Saridewi, N (2017). Biosynthesis nnd characterization of ZnO nanoparticles with extract of green seaweed *Caulerpa* sp. *Jurnal Perikanan Universitas Gadjah Mada*, *19(1)*: 17-28. DOI: 10.22146/JFS.24488.

Pinto, L F; Montaño, A M; González, C P and Barón, G C (2019). Removal of Rhodamine B in wastewater from the textile industry using geopolymeric material. *J. Phys: Conf. Series*, *1386(1)*: 012040. DOI: 10.1088/1742-6596/1386/1/012040.

Rahayu, D P and Nurhayati, E (2023). Pemanfaatan activated spent bleaching earth sebagai adsorben untuk menyisihkan Rhodamine-B: Studi adsorpsi secara batch. *Envirotek: Jurnal Ilmiah Teknik Lingkungan*, *15(1)*: 91-97. DOI: 10.33005/envirotek.v15i1.41.

Rajendrachari, S; Taslimi, P; Karaoglanli, A C; Uzun, O; Alp, E and Jayaprakash, G K (2021). Photocatalytic degradation of Rhodamine B (RhB) dye in waste water and enzymatic inhibition study using cauliflower shaped ZnO nanoparticles synthesized by a novel One-pot green synthesis method. *Arab. J. Chem.*, *14(6)*: 103180. DOI: 10.1016/J.ARABJC.2021.103180.

Rizqiyah, M; Susanti, D; Pramata, A D and Nurhayati, E (2022). *Analisis pengaruh temperatur pada proses aktivasi material komposit spent bleaching earth/zinc oxide (SBE/ZnO) dengan metode pirolisis terhadap kemampuan degradasi Rhodamine B*. Undergraduate Thesis, Institut Teknologi Sepuluh Nopember (ITS).

Sabour, M R and Shahi, M (2018). Spent bleaching earth recovery of used motor-oil refinery. *Civ. Eng. J.*, *4(3)*: 572-584. DOI: 10.28991/cej-0309116.

Sani, H A; Ahmad, M B; Hussein, M Z; Ibrahim, N A; Musa, A and Saleh, T A (2017). Nanocomposite of ZnO with montmorillonite for removal of lead and copper ions from aqueous solutions. *Proc. Safety Enviro. Prot.*, *109*: 97-105. DOI: 10.1016/j.psep.2017.03.024.

Saputra, E; Utama, P S; Irdoni, H S; Simatupang, M D V; Prawiranegara, B A; Abid, H R and Muraza, O (2020). Spent bleaching earth supported $CeFeO_3$ perovskite for visible light photocatalytic oxidation of methylene blue. *J. Appl. Mater. Tech.*, *1(2)*: 81-87. DOI: 10.31258/JAMT.1.2.81-87.

Saraswati, I; Diantariani, N and Suarya, P (2015). Fotodegradasi zat warna tekstil congo red dengan fotokatalis ZnO-arang aktif dan sinar ultraviolet (UV). *J. Kim.*, *9(2)*: 175-182.

Sawicki, B; Tomaszewicz, E; Piątkowska, M; Groń, T; Duda, H and Górny, K (2016). Correlation between the band-gap energy and the electrical conductivity in $MPr_2W_2O_{10}$ tungstates (Where M= Cd, Co, Mn). *Acta Pyhs. Pol. A*, *129(1-A)*: A94-96. DOI: 10.12693/APhysPolA.129.A-94.

Septiani, U; Bella, I and Syukri, D (2014). Pembuatan dan karakterisasi katalis ZnO/karbon aktif dengan metode solid state dan uji aktifitas katalitiknya pada degradasi Rhodamin B. *Jurnal Riset Kimia*, *7(2)*: 180-180. DOI: 10.25077/JRK.V7I2.186.

Singh, J P; Lim, W C; Won, S O; Song, J and Chae, K H (2018). Synthesis and characterization of some alkaline-earth-oxide nanoparticles. *J. Kor. Phys. Soc.*, *72(8)*: 890-899. DOI: 10.3938/JKPS.72.890/METRICS.

Slamet, A; Yulikasari, A; Nurhayati, E and Cornelio, F X F (2021). Pengaruh cahaya ambient terhadapt efektivitas penyisihan rhodamine b menggunakan material komposite spent bleaching earth-ZnO. *Jurnal Purifikasi*, *20(2)*: 58-63. DOI: 10.12962/j25983806.v20.i2.438.

Sukiran, M A; Loh, S K and Bakar, N A (2018). Conversion of pre-treated oil palm empty fruit bunches into bio-oil and bio-char via fast pyrolysis. *J. Oil Palm Res.*, *30(1)*: 121-129. DOI: 10.21894/jopr.2018.0006.

Trivana, L; Sugiarti, S and Rohaeti, E (2015). Sintesis zeolit dan komposit zeolit/TiO_2 dari kaolin serta uji adsorpsi-fotodegradasi biru metilena. *ALCHEMY Jurnal Penelitian Kimia*, *11(2)*: 147-162.

Uphadyaya, G S and Dube, R K (1985) *Problems in Metallurgical Thermodynamics and Kinetics.* 1st edition. Pergamon Press, Oxford, England. p. 203-207.

Wafti, N S A; Yoo, C K; Lin, S W; Yaw, T C S and Abdullah, L C (2011). Regeneration and characterization of spent bleaching clay. *J. Oil Palm Res.*, *23*: 999-1004.

Yousif, E and Haddad, R (2013). Photodegradation and photostabilization of polymers, especially polystyrene: Review. *SpringerPlus 2(1):* 1-32. DOI: 10.1186/2193-1801-2-398.

Yulikasari, A; Nurhayati, E; Utama, W and Warmadewanthi, I (2022). Characterization of spent bleaching earth as an adsorbent material for dye removal. *J. Ecol. Eng.*, *Vol. 23(4)*: 96-104. DOI: 10.12911/22998993/146353.

Yulikasari, A; Nurhayati, E and Warmadewanthi, I (2023). *Aplikasi komposit fotokatalis SBE/ZnO pada proses ozonasi katalitik untuk mendegradasi Rhodamine B*. Master Thesis, Institut Teknologi Sepuluh Nopember (ITS), Surabaya - Indonesia.

Yustinah, Y; Hudzaifah, H; Aprilia, M and Ab, S (2019). Kesetimbangan adsorpsi logam berat (Pb) dengan adsorben tanah diatomit secara batch. *Jurnal Konversi*, *9(1)*: 17-27. DOI: 10.24853/konversi.9.1.12.

Zhang, W; Lan, Y; Ma, M; Chai, S; Zuo, Q; Kim, K H and Gao, Y (2020). A novel chitosan–vanadium-titanium-magnetite composite as a superior adsorbent for organic dyes in wastewater. *Enviro. Inter.*, *142(105798)*: 1-12. DOI: 10.1016/J.ENVINT.2020.105798.